Laser Reference Sensor Alignment Tracking and Star Observations

Noah H. Smith,* Sungkoo Bae,† and Bob E. Schutz‡

University of Texas at Austin, Austin, Texas 78712

The laser reference sensor is the central instrument in the Ice, Cloud, and land Elevation Satellite 2 laser pointing knowledge system, simultaneously observing stars and the altimetry laser in a single instrument coordinate frame. The star observations are relatively sparse, with a predicted brightness cutoff near visual magnitude 5, and their density varies significantly across the sky. There are star gaps of up to approximately 200 s, and areas of the sky with 20 simultaneously observable stars. The star observations are augmented with observations from two spacecraft star trackers using an alignment filter. The filter tracks the motion of the laser reference sensor relative to the spacecraft. Monte Carlo simulation is used to characterize the effects of various magnitude cutoffs, types of alignment variations, and regions of the sky on alignment tracking and overall pointing knowledge performance. Multiple model adaptive estimation is used to map alignment process noise filter tuning with respect to the input parameters. The results include pointing knowledge uncertainty predictions over an input parameter space of three star brightness cutoffs, two types of alignment variations, and three alignment variation amplitudes. The results also map pointing uncertainty to regions of the sky and individual stars.

Nomenclature

$\mathbf{A}_i^{\text{ATLAS}}$	=	true reference platform attitude
$\mathbf{A}_i^b$	=	estimated reference platform and body frame attitude
$\mathbf{A}_{\text{ATLAS}}^{\text{LRS}}$	=	constant reference alignment
$\mathbf{A}_i^{\text{LRS}}$	=	true laser reference sensor attitude
$\hat{\mathbf{A}}_i^{\text{LRS}}$	=	estimated laser reference sensor attitude
a	=	attitude error rotation vector, rad
b	=	gyro rate bias vector, rad/s
a_{LRS}	=	true alignment rotation vector, rad
$\hat{a}_{\text{LRS}}$	=	estimated alignment rotation vector, rad
e	=	alignment error rotation vector, rad
$\mathbf{H}$	=	sensitivity matrix
$h(u)$	=	h, v coordinates of a star unit vector (star observation model)
$\mathbf{K}$	=	Kalman gain matrix
$\mathbf{P}$	=	state covariance matrix
$\mathbf{Q}$	=	process noise covariance matrix
$\mathbf{R}$	=	measurement noise covariance matrix
$\mathbf{R}(a)$	=	state transition submatrix
$\mathbf{S}(a)$	=	state transition submatrix
u_{obs}	=	simulated star observation unit vector
u_{ref}	=	reference star catalog unit vector in the celestial frame
x	=	state vector
α_{node}	=	right ascension offset applied to star catalog unit vectors, rad
Δy	=	star observation residual in h, v coordinates
$\eta(t)$	=	zero-mean Gaussian noise process
$\omega(t)$	=	angular rate vector, rad/s
$\omega_g(t)$	=	gyro output angular rate vector, rad/s
Φ	=	state transition matrix
$\sigma_{\Delta b}$	=	scaling factor in the random walk of simulated rate observations

*Postdoctoral Fellow, Center for Space Research. Member AIAA.
†Research Scientist Engineer, Center for Space Research. Member AIAA.
‡Professor and Associate Director, Center for Space Research. Fellow AIAA.

I. Introduction

THE Ice, Cloud, and land Elevation Satellite 2 (ICESat-2) pointing knowledge system centers on the laser reference sensor (LRS) that simultaneously observes stars and the altimetry lasers in the LRS coordinate frame [1–4]. Ideally, the LRS attitude and, by extension, the pointing of the lasers in the celestial frame are determined by the star observations. In practice, estimation of the LRS attitude from imperfect observations is the key factor in laser pointing knowledge.

The ICESat-2 LRS is very different from the ICESat-1 LRS [1]. The ICESat-1 LRS was a relatively simple instrument and dependent on collocated external components (gyro unit, instrument star tracker, laser profiler array, and collimated reference source). The ICESat-2 LRS is more sophisticated and intended to be independent. In particular, it is intended to provide continuous observations of a relatively large number of stars, comparable to the current generation of star trackers, except when blinded by the Sun. Ideally, it should be sensitive enough to track stars at least as dim as approximately visual magnitude 6, resulting in 5000–6000 trackable stars with a fairly dense and uniform distribution across the sky.

During testing of LRS hardware components, problems were found with the originally specified detector. The replacement detector results in a lower sensitivity of approximately visual magnitude 5, with 1000–1500 trackable stars. Pointing knowledge requirements are unchanged, but the LRS star observations are relatively sparse, defined here as meaning the number of trackable stars goes to zero in some regions of the sky (regardless of sun, moon, and Earth effects).

The objective of this paper is to predict pointing knowledge performance where the observations are sparse and the requirement is difficult (better than 0.4 arcsec 1σ). We are not aware of a similar study in the open literature, but sparse LRS star observations increase the importance of tracking the relative alignments of the attitude sensors, which is a significant topic in the literature. The pointing knowledge processor used here builds on alignment filtering work published over the last 15 years [5–10]. Variation of the LRS alignment, relative to the other attitude sensors, is referred to here as LRS motion, and the difference between the true and estimated motion is referred to as LRS alignment tracking error.

A contribution of this paper is the way Monte Carlo simulation is used to estimate LRS alignment tracking errors and overall pointing knowledge performance for a range of LRS sensitivities and LRS motions. Monte Carlo simulation is demonstrated to be an effective method for mapping problem regions of the sky, where tracking errors increase due to sparse observations. Another contribution is the

use of multiple-model adaptive estimation to find LRS alignment state process noise estimates as a function of both LRS sensitivity and motion.

II. Background and Definitions

ICESat-2 is scheduled for launch in 2016 and intended to operate for at least three years. The objective is laser altimetry using the Advanced Topographic Laser Altimeter System (ATLAS) to measure ice sheet mass elevation, sea ice freeboard, land topography, and vegetation characteristics. Highly accurate measurements of the surface elevation at each laser footprint are required [11–14]. The location of a footprint and its associated elevation are obtained by combining the geocentric position vector of ATLAS, the laser pointing vector, and laser pulse time-of-flight measurements. The accuracy requirement for surface elevation is equivalent to a laser pointing knowledge accuracy of 1.5 arcsec 1σ for each of the 6 laser beams.

Figure 1 shows ATLAS and its pointing knowledge sensors. The LRS is mounted vertically through the ATLAS optical bench and consists of two imagers joined back-to-back, with a star tracker pointed at the zenith and a laser tracker pointed at the nadir observing the altimetry laser beams. The LRS star tracker sunshade is prominent in Fig. 1. Because the LRS is intended to operate independently, it is not collocated with the gyro unit and two spacecraft star trackers (SST), which are mounted on a small platform, referred to as the ATLAS reference platform and defining the ATLAS reference frame in Fig. 1.

Structurally, the gyro unit is distant from the LRS. The LRS is attached to the ATLAS optical bench by three mounting brackets, which are expected to flex. The gyro unit is on the reference platform, which is attached to the ATLAS optical bench by its own three mounting brackets, and the ATLAS optical bench itself is flexing between the LRS and reference platform, at least to some degree. This structural separation between the gyro unit and LRS is of first-order significance, as demonstrated by contrasting the situation with ICESat-1. On ICESat-1, the gyro unit and LRS were collocated. The alignment between their instrument frames was relatively stable and, in practice, gyro telemetry could be used to propagate an adequate LRS attitude estimate over orbital time scales [15–19]. We consider this situation, based on colocation of a science instrument and gyro unit, to be normal and what is generally expected.

In the ICESat-2 case, for pointing knowledge purposes the overall situation can be approximated as two rigid bodies, the LRS and reference platform, which are constrained by the intervening mounting brackets and optical bench to have some degree of alignment stability. The reference platform is designed specifically for thermal isolation and stability. As a first-order rigid body model, internal alignments within the reference platform (between the gyro unit and SSTs) are approximated as constant. The objective is to simultaneously track the reference platform attitude and LRS alignment: in other words, the rotations from the celestial frame to the reference platform frame, and from the reference platform frame to the LRS frame.

The LRS star tracker has a $12° \times 12°$ field of view and outputs centroid and brightness measurements at 10 Hz. It can track up to 30 stars simultaneously, but with its sensitivity limitations it normally tracks on the order of 5 stars. The SSTs output estimated attitude quaternions at 10 Hz. The gyro unit has four sense-axes arranged in a pyramid geometry and outputs angular increments about each sense-axis at 100 Hz. Flight telemetry samples the gyro unit output at 50 Hz.

Attitude and alignment rotations are represented by rotation matrices $\mathbf{A}$ or their quaternion equivalents $q(\mathbf{A})$. Small rotations are represented by rotation vectors $\boldsymbol{a}$ or their equivalents $\mathbf{A}(\boldsymbol{a})$ or $q(\boldsymbol{a})$, where a rotation vector is defined as an Euler axis and angle $\boldsymbol{a} = \phi\boldsymbol{e}$; $|\boldsymbol{e}| = 1$ [20]. For quaternions, $\otimes$ is the multiplication operator and q^* is the conjugate of q. All quaternions are normalized $q = q/|q|$ to unit length. A quaternion can be represented as $q = [\boldsymbol{q}^T \quad q_4]^T$ with a three component vector part $\boldsymbol{q} = [q_1 \quad q_2 \quad q_3]^T$ and a scalar component q_4. The cross-product matrix $[\boldsymbol{a}\times]$ is defined by $[\boldsymbol{a}\times]\boldsymbol{b} = \boldsymbol{a} \times \boldsymbol{b}$.
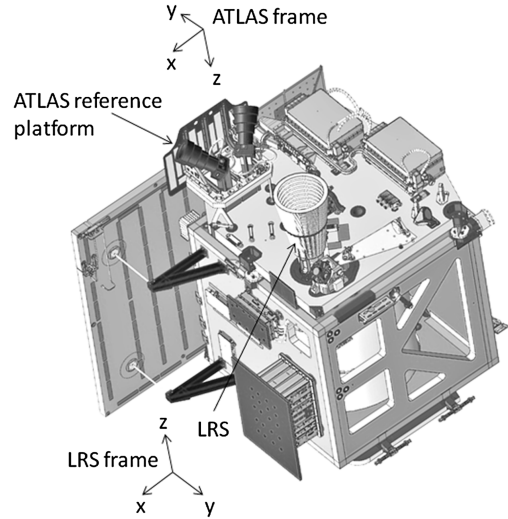

Fig. 1 ATLAS, the LRS, and the reference platform.

III. Reference Platform Attitude Tracking

The performance results presented here are based on Monte Carlo simulation of the first-order rigid body model, in which pointing knowledge involves three objects: reference platform attitude, LRS alignment, and laser vectors in the LRS frame. The first-order model represents the most significant performance factors and allows secondary complexities to be represented as internal alignment uncertainties and higher-order corrections.

At each point in simulated time there are two reference platform attitudes and two LRS alignments: the truth from the simulation, and an estimate from processing simulated sensor observations. The term "tracking" refers here to the difference between estimated and true values, represented by a tracking error time series and rms tracking error statistics. The focus of the results section is attitude and alignment tracking, with the assumption that in practice the laser vector observations are well calibrated and pointing knowledge is a function of attitude and alignment tracking performance.

A. Simulation Truth

The truth time series is referred to as SIMV9 (Simulation Version 9) and serves as a baseline throughout the ICESat-2 orbit, pointing, and geolocation knowledge group. SIMV9 is designed to provide a realistic representation of normal pointing, ocean scans, around the world scans, target scans, and the transitions between. It consists of a time series of true attitudes $\mathbf{A}_i^{\text{ATLAS}}(t_k)$ at 1 s intervals over 1 day. Angular rates $\boldsymbol{\omega}_k$ are derived from $\mathbf{A}_i^{\text{ATLAS}}(t_k)$ and both are resampled to 0.1 s intervals to match the fundamental frequency of the star tracker observations and the overall tracking problem.

The $\boldsymbol{\omega}_k$ are tested to ensure that they adequately represent the true rates and ideal gyro unit observations. They should provide the best practical attitude tracking possible and a lower-bound on numerical errors in state propagation within the processor. Attitude tracking using ideal gyro observations alone propagates the time series of estimates $\mathbf{A}_i^b(t_k)$ forward from the initial $\mathbf{A}_i^b \equiv \mathbf{A}_i^{\text{ATLAS}}(t_0)$ using $\boldsymbol{\omega}_k$. If significant differences from $\mathbf{A}_i^{\text{ATLAS}}(t_k)$ accumulate in $\mathbf{A}_i^b(t_k)$, then the $\boldsymbol{\omega}_k$ are not a valid representation of the true rates and ideal gyro observations. The attitude change from t_k to t_{k+1} is approximated by the rotation vector $\boldsymbol{a}_k = (t_{k+1} - t_k)\boldsymbol{\omega}_k$ and equivalent quaternion $q(\boldsymbol{a}_k) = [\boldsymbol{a}_k^T/2 \quad 1]^T$. The estimated attitude at t_{k+1} is $q(\mathbf{A}_i^b)_{k+1} = q(\boldsymbol{a}_k) \otimes (\mathbf{A}_i^b)_k$. The estimates are calculated sequentially and the error at each step is represented by the quaternion $q_{\text{err}} = q(\mathbf{A}_i^b) \otimes q(\mathbf{A}_i^{\text{ATLAS}})^*$ and equivalent rotation vector $\boldsymbol{a}_{\text{err}} = 2[q_{\text{err},1} \quad q_{\text{err},2} \quad q_{\text{err},3}]^T$.

Figures 2–4 show $\boldsymbol{\omega}_k$ and abs($\boldsymbol{a}_{\text{err}}$) for the resampled 10 Hz SIMV9 data. In Fig. 2 the two ocean scan maneuvers (A and C), target scans (B), and around the world scan (D) are apparent in the roll rate time series. The maneuver sequence is not representative of actual on-orbit operations but is convenient for studying scans and transitions.
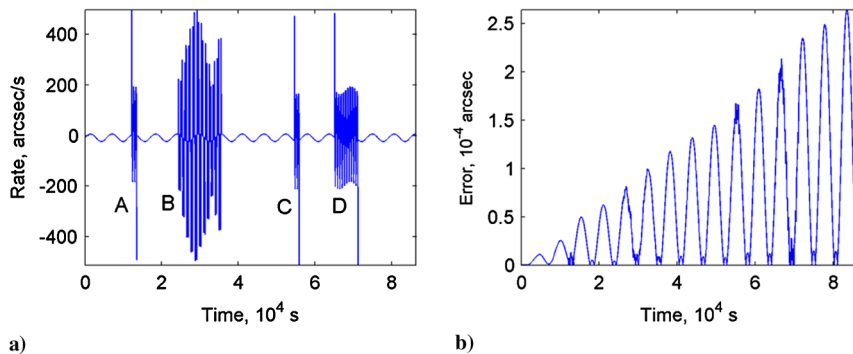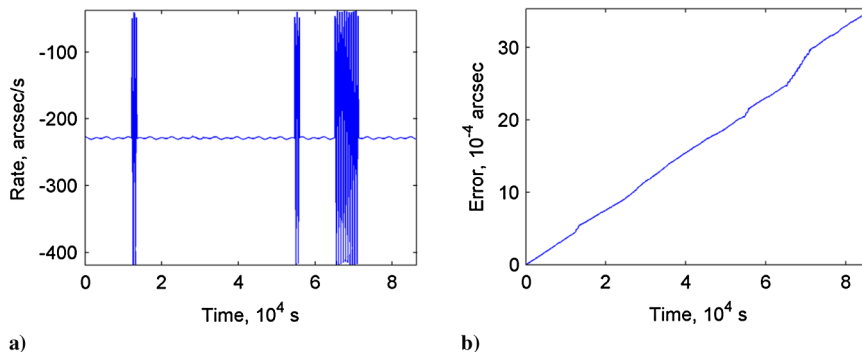
Fig. 2   Roll a) ω_k and b) abs(a_{err}).

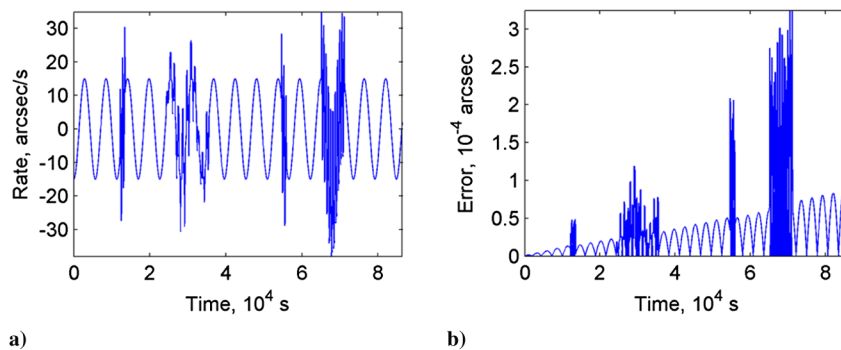**Fig. 3   Pitch a) ω_k and b) abs(a_{err}).**

Fig. 4   Yaw a) ω_k and b) abs(a_{err}).

Attitude tracking errors are on the order of 3×10^{-3} arcsec/day or less with rms values of 9×10^{-5} arcsec in roll, 2×10^{-3} arcsec in pitch, and 6×10^{-5} arcsec in yaw. This indicates that the ω_k values are an adequate representation of the ideal gyro unit observations, and that the lower-bound on attitude tracking errors is much smaller than the errors from realistic gyro observations, which are more than four orders of magnitude larger at approximately 5 arcsec/h.

The results section focuses on roll tracking performance, and is representative of pitch tracking performance. Roll motion is equivalent to cross-track pointing and of first importance for laser spot geolocation and ICESat-2 science. The rate and acceleration variations are highest in roll as the calibration and target scans sweep the lasers across the ground track, particularly during target scans that are effectively pure roll (Figs. 2–4). Peak acceleration magnitudes are approximately 140 arcsec/s^2 as shown in Fig. 5.

Two test cases used below for attitude tracking performance analysis are taken from the ocean scan shown in the left plot of Fig. 5. The baseline case with nadir pointing angular rates and small angular accelerations is from 12,000 to 12,065 s, just before the first acceleration peak. An upper-bound case with peak angular accelerations covers the first acceleration peak from 12,135 to 12,220 s.

B.   States and Observations

Simulated sensor observations are generated from the truth time series, including the effects of LRS motion, deterministic errors, and noise. The simulated sensor observations are then processed as artificial flight telemetry. Monte Carlo simulation runs for different LRS sensitivities and different regions of the sky provide information about the observation characteristics and the relationship between sensitivity and tracking performance. The results from multiple simulation runs are combined to characterize attitude and alignment tracking performance.

The processor is a Kalman filter that estimates reference platform attitude, gyro rate bias, and LRS alignment and is referred to here as an alignment filter [5–7]. Alignment filtering simultaneously predicts the measurements from all three star trackers (the LRS star tracker and the two SSTs). The sparse LRS observations are effectively combined with the observations from the other two trackers. The measurement residuals are used to update the filter states, which represent the body frame attitude and time-varying corrections to the LRS reference alignment. The SSTs are tied to the body frame by constant reference alignments. The combined states represent the attitudes of all three trackers. This type of alignment filtering is applicable to any configuration of vector sensors; if the vector
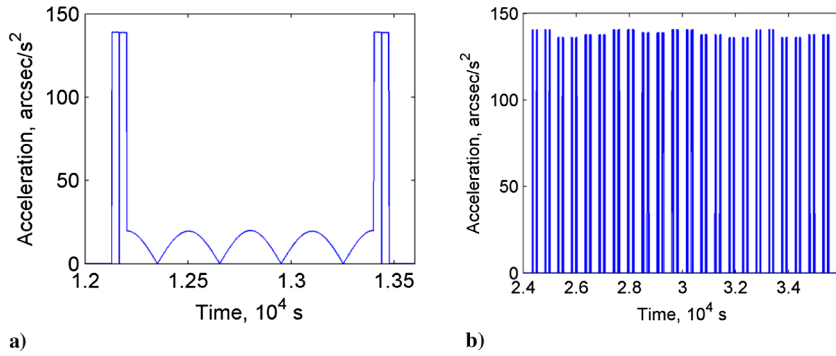
Fig. 5   Roll acceleration magnitudes during a) ocean scan A and b) target scan B from Fig. 2.

observations can be predicted, then the sensor alignment estimates can be updated.

There are two ATLAS reference platform attitudes: the simulation truth $\mathbf{A}_i^{\text{ATLAS}}(t)$, and an estimate $\mathbf{A}_i^b(t)$. Any expression that includes $\mathbf{A}_i^{\text{ATLAS}}(t)$ refers to simulation truth, and any expression that includes $\mathbf{A}_i^b(t)$ refers to estimated values. For example, $\mathbf{A}_i^{\text{LRS}}(t) = \mathbf{A}[\boldsymbol{a}_{\text{LRS}}(t)]\mathbf{A}_{\text{ATLAS}}^{\text{LRS}}\mathbf{A}_i^{\text{ATLAS}}$ refers to the true LRS attitude and alignment, whereas $\hat{\mathbf{A}}_i^{\text{LRS}}(t) = \mathbf{A}[\boldsymbol{a}_{\text{LRS}}(t)]\mathbf{A}_b^{\text{LRS}}\mathbf{A}_i^b(t)$ refers to their estimated values.

The true SST attitudes are modeled as the product of a constant reference alignment $\mathbf{A}_{\text{ATLAS}}^{\text{SST}}$ and the reference platform attitude $\mathbf{A}_i^{\text{ATLAS}}(t)$:

$$\mathbf{A}_i^{\text{SST1}}(t) = \mathbf{A}_{\text{ATLAS}}^{\text{SST1}}\mathbf{A}_i^{\text{ATLAS}}(t) \tag{1}$$

$$\mathbf{A}_i^{\text{SST2}}(t) = \mathbf{A}_{\text{ATLAS}}^{\text{SST2}}\mathbf{A}_i^{\text{ATLAS}}(t) \tag{2}$$

Time-varying corrections to the reference alignments $\mathbf{A}_{\text{ATLAS}}^{\text{SST}}$ are not modeled or estimated, and the SST coordinate frames are effectively identified with the reference platform frame. A time-varying rotation vector $\boldsymbol{a}_{\text{LRS}}(t)$ representing small alignment corrections is included in the attitude models for the LRS:

$$\mathbf{A}_i^{\text{LRS}}(t) = \mathbf{A}[\boldsymbol{a}_{\text{LRS}}(t)]\mathbf{A}_{\text{ATLAS}}^{\text{LRS}}\mathbf{A}_i^{\text{ATLAS}}(t) \tag{3}$$

where $\mathbf{A}_{\text{ATLAS}}^{\text{LRS}}$ is the LRS reference alignment. The state vector is

$$\boldsymbol{x}(t) = [\,\boldsymbol{a}(t)^T \quad \boldsymbol{b}(t)^T \quad \boldsymbol{a}_{\text{LRS}}(t)^T\,]^T \tag{4}$$

where $\boldsymbol{a}(t)$ is the attitude error rotation vector and $\boldsymbol{b}(t)$ is the rate bias. These states are estimated sequentially using an alignment filter based on the standard attitude filter, referred to by [20] as the Multiplicative Extended Kalman Filter. The description here follows [6,7,20,21].

The filter performs unconstrained estimation of the rotation vector $\boldsymbol{a}(t)$ during each measurement update phase while maintaining the overall body frame attitude estimate in the unit-norm reference attitude quaternion $q_b(t)$ with $\hat{\mathbf{A}}_i^b(t) = \mathbf{A}[q_b(t)]$. The true attitude $q_{\text{ATLAS}}(t)$ is modeled as $q_{\text{ATLAS}}(t) = q[\boldsymbol{a}(t)] \otimes q_b(t)$ [20]. The measurement update phase assigns a finite value $\hat{\boldsymbol{a}}_+$ to $\hat{\boldsymbol{a}}(t)$ while the estimated quaternion retains its preupdate value q_{b-}. The update information is moved from $\hat{\boldsymbol{a}}_+$ to a postupdate reference $q_{b,+}$, and $\hat{\boldsymbol{a}}(t)$ is reset to zero so that $q(\hat{\boldsymbol{a}}_+) \otimes q_{b,-} = q(\mathbf{0}) \otimes q_{b,+}$.

The covariance matrix $\mathbf{P}$ is given by

$$\mathbf{P}_{9\times9} = E\{(\boldsymbol{x} - \hat{\boldsymbol{x}})(\boldsymbol{x} - \hat{\boldsymbol{x}})^T\} = \begin{bmatrix} \mathbf{P}_a & \mathbf{P}_{ab} & \\ \mathbf{P}_{ab} & \mathbf{P}_b & \\ & & \mathbf{P}_{\text{LRS}} \end{bmatrix} \tag{5}$$

where $\mathbf{P}$ is partitioned into 3×3 attitude $\mathbf{P}_a$, rate $\mathbf{P}_b$, correlation $\mathbf{P}_{ab}$, and alignment $\mathbf{P}_{\text{LRS}}$ submatrices. In the continuous-time linearized state equation given by

$$\begin{bmatrix} \delta\dot{\boldsymbol{a}} \\ \delta\dot{\boldsymbol{b}} \\ \delta\dot{\boldsymbol{a}}_{\text{LRS}} \end{bmatrix} = \begin{bmatrix} -[\boldsymbol{\omega}_{\text{ref}}\times] & \mathbf{I}_{3\times3} & \\ \mathbf{0}_{3\times3} & \mathbf{0}_{3\times3} & \\ & & \mathbf{0}_{3\times3} \end{bmatrix} \begin{bmatrix} \delta\boldsymbol{a} \\ \delta\boldsymbol{b} \\ \delta\boldsymbol{a}_{\text{LRS}} \end{bmatrix} + \mathbf{I}_{9\times9} \begin{bmatrix} \boldsymbol{\eta}_{\text{arw}} \\ \boldsymbol{\eta}_{\text{rrw}} \\ \boldsymbol{\eta}_{\text{LRS}} \end{bmatrix} \tag{6}$$

the rate bias $\delta\boldsymbol{b}$ and alignment error $\delta\boldsymbol{a}_{\text{LRS}}$ are driven by process noise alone, with $E\{\boldsymbol{\eta}_{\text{arw}}\boldsymbol{\eta}_{\text{arw}}^T\} = \sigma_{\text{arw}}^2\mathbf{I}$, $E\{\boldsymbol{\eta}_{\text{rrw}}\boldsymbol{\eta}_{\text{rrw}}^T\} = \sigma_{\text{rrw}}^2\mathbf{I}$, and $E\{\boldsymbol{\eta}_{\text{LRS}}\boldsymbol{\eta}_{\text{LRS}}^T\} = \sigma_{\text{LRS}}^2\mathbf{I}$. The discrete-time process noise matrix for a propagation interval $\Delta t = t_{k+1} - t_k$ is given by

$$\mathbf{Q}_k = \begin{bmatrix} (\sigma_{\text{awn}}^2 + \Delta t\sigma_{\text{arw}}^2 + (\Delta t^3/3)\sigma_{\text{rrw}}^2)\mathbf{I} & (\Delta t^2/2)\sigma_{\text{rrw}}^2\mathbf{I} & \\ (\Delta t^2/2)\sigma_{\text{rrw}}^2\mathbf{I} & \Delta t\sigma_{\text{rrw}}^2\mathbf{I} & \\ & & \Delta t\sigma_{\text{LRS}}^2\mathbf{I} \end{bmatrix} \tag{7}$$

The LRS alignment process noise σ_{LRS} is estimated using multiple model adaptive estimation as described in Sec. IV.B.

C. Simulated Rate Observations and State Propagation

Simulated gyro unit rate observations are generated by adding measurement errors to the ideal rate time series $\boldsymbol{\omega}_k$, producing an observed rate time series $\boldsymbol{\omega}_{g,k}$. Gyro noise and rate bias are modeled by short-term variations and long-term trends in the rate error $\boldsymbol{\omega}_{g,k} - \boldsymbol{\omega}_k$. A basic model of the errors is $\boldsymbol{\omega}_{g,k} = \boldsymbol{\omega}_k + \boldsymbol{b}_k + \boldsymbol{\eta}_{\text{awn}}$, where $\boldsymbol{\eta}_{\text{awn}}$ is short-time-scale angular white noise in the gyro output with $E\{\boldsymbol{\eta}_{\text{awn}}\boldsymbol{\eta}_{\text{awn}}^T\} = \sigma_{\text{awn}}^2\mathbf{I}$. Random values $\Delta\boldsymbol{b}_k$ are added sequentially to the rate bias at each time step $\boldsymbol{b}_k = \boldsymbol{b}_{k-1} + \Delta\boldsymbol{b}_k$ with $E\{\Delta\boldsymbol{b}_k\Delta\boldsymbol{b}_k^T\} = \sigma_{\Delta b}^2\mathbf{I}$. The parameter $\sigma_{\Delta b}$ characterizes the random walk of $\boldsymbol{b}_k$.

Gyro unit observation uncertainties are commonly characterized using three parameters: angular white noise σ_{awn}, angular random walk variance σ_{arw}, and rate random walk variance σ_{rrw}. Uncertainties for the ICESat-2 gyro unit are specified as $\sigma_{\text{awn}} = 1.454 \times 10^{-8}$ rad/Hz$^{1/2}$, $\sigma_{\text{arw}} = 7.272 \times 10^{-10}$ rad/s$^{1/2}$, and $\sigma_{\text{rrw}} = 2.424 \times 10^{-11}$ rad/s$^{3/2}$. The angular parameters σ_{awn} and σ_{arw} are associated with short time scales and noise, and the rate parameter σ_{rrw} is associated with longer time scales and rate bias. The growth in rate uncertainty is characterized by $\sqrt{t}\sigma_{\text{rrw}}$ and this value can be used as the basis for a model of $\Delta\boldsymbol{b}_k$, resulting in a parameter estimate of $\sigma_{\Delta b} = 7.6 \times 10^{-12}$ rad/s. However, σ_{rrw} does not represent all of the factors involved in overall bias stability.

Another specified characteristic of the gyro unit is a bias stability of approximately 5 arcsec/h 1σ. Monte Carlo simulation is used to find the $\sigma_{\Delta b}$ that results in an attitude tracking error of approximately 5 arcsec 1σ after 1 h of propagation. A set of $m = 12$ hypothetical $\sigma_{\Delta b}$ values is tested by using each value for a set of $n = 90$ 1 h attitude propagation runs, resulting in $mn = 1080$ total runs. The random walk of the rate bias is unique in each run, and the final attitude errors of all 90 runs for a given $\sigma_{\Delta b}$ value represent its error distribution. The $\sigma_{\Delta b}$ whose error distribution sigma is closest to 5 arcsec is the best parameter estimate. Figure 6 shows the error sigmas for the $12\sigma_{\Delta b}$ values, and demonstrates that $\sigma_{\Delta b} = 8 \times 10^{-11}$ rad/s results in an attitude tracking error of 5 arcsec/h 1σ.
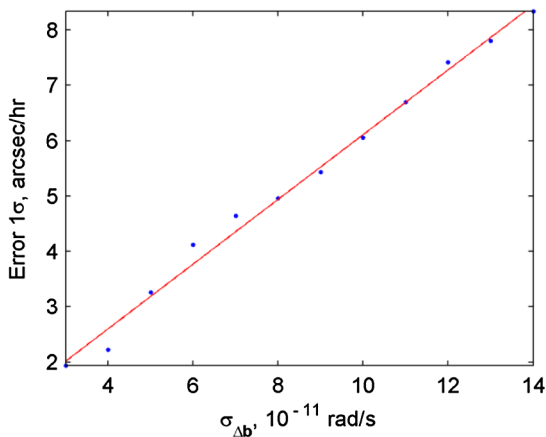
Fig. 6 Attitude tracking error per hour of propagation for various $\sigma_{\Delta b}$ values.

For filter state propagation, the gyro unit outputs time-tagged angular increments that are used to compute the rate observations ω_g. The filter models the rate as $\omega = \omega_g + b + \eta_{\mathrm{arw}}$, where $\mathrm{d}b/\mathrm{d}t = \eta_{rrw}$. The state propagation rotation vector is $a = \Delta t(\omega_g + b)$, where the time interval is short enough that ω_g is approximately constant. Attitude propagation when the assumption of approximately constant ω is not valid is discussed in [22]. The discrete-time state transition matrix is given by

$$\mathbf{\Phi}_k = \begin{bmatrix} \mathbf{R}(a) & \Delta t \mathbf{S}(a) & \\ \mathbf{0}_{3\times 3} & \mathbf{I}_{3\times 3} & \\ & & \mathbf{I}_{3\times 3} \end{bmatrix} \qquad (8)$$

where $\mathbf{R}(a) = \mathbf{I} \cos a - [a\times]\sin a/a + aa^T(1 - \cos a)/a^2$ and $\mathbf{S}(a) = \mathbf{I}\sin a/a - [a\times](1 - \cos a)/a^2 + aa^T(a - \sin a)/a^3$. The propagated attitude estimate and state are $q_{b,k+1} = q(a_p) \otimes q_{b,k}$ and $x_{k+1} = x_k$, and the propagated covariance is $\mathbf{P}_{k+1} = \mathbf{\Phi}_k \mathbf{P}_k \mathbf{\Phi}_k^T + \mathbf{Q}_k$.

D. Simulated Attitude Observations and Attitude Updates

The effective observations output by the SSTs are quaternions and are used to directly correct the estimated attitude state. Attitude tracking performance depends on the error characteristics of these quaternion observations over all but the shortest time scales, where rate and propagation errors dominate. The attitude observation errors are modeled here as white noise in the quaternions. Simulated attitude observations and attitude updates are discussed here for SST1, and the SST2 case is identical.

Simulated observations for SST1 are given by $q_i^{\mathrm{SST1}} = q(\eta_{\mathrm{SST}}) \otimes q_{\mathrm{ATLAS}}^{\mathrm{SST1}} \otimes q_i^{\mathrm{ATLAS}}$, where η_{SST} is a rotation vector representing attitude observation uncertainties $R = E\{\eta_{\mathrm{SST}}\eta_{\mathrm{SST}}^T\} = \mathrm{diag}([\sigma_{\mathrm{SST}x}^2 \quad \sigma_{\mathrm{SST}y}^2 \quad \sigma_{\mathrm{SST}z}^2])$ and the constant reference alignment for SST1 is $q_{\mathrm{ATLAS}}^{\mathrm{SST1}}$. The observation uncertainties are specified by the manufacturer as $\sigma_{\mathrm{SST}x} = \sigma_{\mathrm{SST}y} = 1.5$ arcsec and $\sigma_{\mathrm{SST}z} = 12.2$ arcsec.
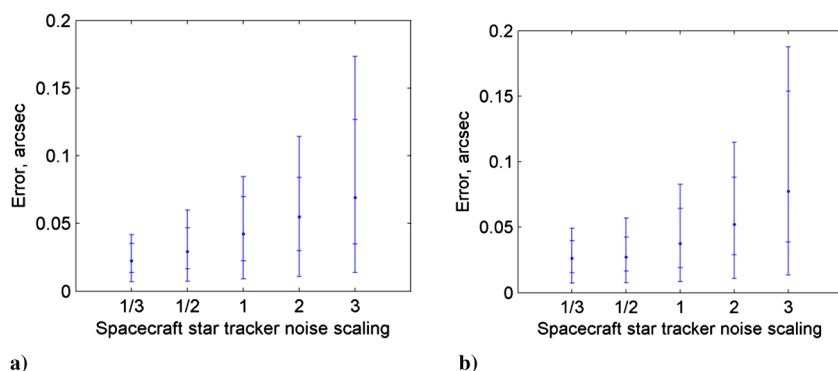
The filter prediction of the SST1 attitude is $q_{\mathrm{ATLAS}}^{\mathrm{SST1}} \otimes q_i^b$, and the observation residual rotation vector Δy is given by $[\Delta y^T/2 \quad q_4]^T = q_i^{\mathrm{SST1}} \otimes (q_{\mathrm{ATLAS}}^{\mathrm{SST1}} \otimes q_i^b)^*$. Attitude updates are performed using the observation sensitivity $\mathbf{H} = [\mathbf{A}_{\mathrm{ATLAS}}^{\mathrm{SST1}} \quad \mathbf{0} \quad \mathbf{0}]$, Kalman gain $\mathbf{K} = \mathbf{P}\mathbf{H}^T(\mathbf{H}\mathbf{P}\mathbf{H}^T + \mathbf{R})^{-1}$, estimated state correction $\Delta x = [\Delta a^T \quad \Delta b^T \quad \Delta a_{\mathrm{LRS}}^T]^T = \mathbf{K}\Delta y$, and covariance update $\mathbf{P}_+ = (\mathbf{I} - \mathbf{K}\mathbf{H})\mathbf{P}_-$. The gyro rate bias update is $b_+ = b_- + \Delta b$ and the updated attitude estimate is $q_{b+} = q(\Delta a) \otimes q_{b-}$.

Two angular acceleration cases are used to characterize attitude tracking errors: a baseline case with nadir pointing angular rates and small angular accelerations, and an upper-bound ocean and target scan case with peak accelerations. For each of the two acceleration cases, five uncertainty scaling factors, 0.33, 0.5, 1, 2, and 3, are applied to σ_{SST}. These 10 cases are used to characterize the sensitivity of attitude tracking error to both acceleration and observation noise. Fifty Monte Carlo simulation runs were performed for each of the 10 cases.

Roll tracking rms error values are given in the results section. Figure 7 shows 0.05, 0.25, 0.5, 0.75, and 0.95 quantile breakdowns of the roll tracking error magnitudes. The central dots are the 0.5 quantiles or median values. The left plot is for the nadir pointing case with small angular accelerations, and the right plot is for the peak acceleration case.

Figure 7 shows that, for the baseline observation noise and both acceleration cases, the median roll tracking error magnitude is approximately 0.05 arcsec. Attitude tracking error magnitudes are similar in both the nadir pointing and peak acceleration cases. With ATLAS reference platform attitude tracking errors on the order of 0.05 arcsec, LRS star observations can be predicted accurately if LRS alignment tracking is also good.

IV. LRS Alignment Tracking

All information for LRS alignment tracking comes from star observations, and they are a primary source of alignment tracking errors, along with filter and numerical errors. The most significant issue is the quantity and distribution of observations across the sky: in other words, the sensitivity of the LRS and its ability to track dim stars. If only bright stars are acquired, there are periods without star observations during which the filter does not receive alignment updates and does not track the LRS alignment.

LRS sensitivity is characterized by the maximum observable instrument magnitude. Instrument and astronomical magnitudes m are unitless ratios defined by the equation

$$m - m_{\mathrm{ref}} = -2.5 \log_{10}(i/i_{\mathrm{ref}}) \qquad (9)$$

where m_{ref} and i_{ref} are reference magnitudes and intensity counts. The predicted instrument magnitude cutoff for the LRS is 5.0 and is referred to here as LRS sensitivity 5.0. The three cases studied in this paper are LRS sensitivities 4.8 (low sensitivity), 5.0 (predicted sensitivity), and 5.2 (high sensitivity).

Another significant issue is deterministic errors and noise in the star observations. Deterministic errors such as distortion are corrected within the processor [2,23,24]. The effects of noise are

a)   b)

Fig. 7 Roll tracking error magnitude distributions for the a) nadir pointing case and b) peak acceleration case.

reduced by observing more stars n, with uncertainty generally scaling by $1/\sqrt{n}$. Low sensitivity reduces n and results in larger uncertainties.

There are also issues with individual stars and their mission catalog records. Normal stars have unbiased observations and catalog records. The exceptions are referred to here as bad stars and become more important as sensitivity decreases [23,25,26]. When the sensitivity is low, there are more periods when only a single star is being tracked. This makes the filter more sensitive to bad stars, because there are fewer normal stars to counteract their effects on filter updates.

The characteristics of the alignment variations can be classed as another source of alignment tracking errors. If the variations are especially complex, it is natural to expect tracking errors to be larger. Monte Carlo simulations are performed for two cases here: a baseline sinusoidal motion, and a more complex case from ICESat-1 flight data.

A. Simulated Star Observations and Alignment Updates

The true LRS attitude is $\mathbf{A}_i^{\mathrm{LRS}}(t) = \mathbf{A}[a_{\mathrm{LRS}}(t)]\mathbf{A}_{\mathrm{ATLAS}}^{\mathrm{LRS}}\mathbf{A}_i^{\mathrm{ATLAS}}(t)$ and the estimated LRS attitude is $\hat{\mathbf{A}}_i^{\mathrm{LRS}}(t) = \mathbf{A}[\hat{a}_{\mathrm{LRS}}(t)]\mathbf{A}_{\mathrm{ATLAS}}^{\mathrm{LRS}}\mathbf{A}_i^b(t)$, where $\mathbf{A}_{\mathrm{ATLAS}}^{\mathrm{LRS}}$ is a constant reference alignment, and $a_{\mathrm{LRS}}(t)$ and $\hat{a}_{\mathrm{LRS}}(t)$ are small rotation vectors representing true and estimated LRS alignments, respectively. LRS alignment tracking error is the rotation vector difference $e(t) = \hat{a}_{\mathrm{LRS}}(t) - a_{\mathrm{LRS}}(t)$. When the attitude tracking error is small so that $\mathbf{A}_i^{\mathrm{ATLAS}} \approx \mathbf{A}_i^b$, the alignment tracking error is approximately equivalent to the quaternion difference $q(\hat{\mathbf{A}}_i^{\mathrm{LRS}}) \otimes q(\mathbf{A}_i^{\mathrm{LRS}})^* \approx [\,\Delta e^T/2 \quad q_4\,]^T$.

Simulated star observations are given by the observation model $y = h(u_{\mathrm{obs}}) = h(\mathbf{A}_i^{\mathrm{LRS}}u_{\mathrm{ref}}) + [\Delta h \quad \Delta v]^T + \eta$, where $h(u) = [u_1/u_3 \quad u_2/u_3]^T \equiv [h \quad v]^T$ and $u = h^{-1}(u) = [h \quad v \quad 1]^T/\|[h \quad v \quad 1]\|$ take advantage of the unit constraint to transform between three-dimensional unit vectors u and the h, v coordinate plane. The star catalog unit vector u_{ref} is expressed in the celestial frame. Deterministic errors are represented by $[\Delta h \quad \Delta v]^T$, and η is noise with an observation covariance of $R = E\{\eta\eta^T\} = \sigma_{\mathrm{obs}}^2 \mathbf{I}_{2\times2}$.

The ascending node of the SIMV9 orbits is near the x-axis of the celestial frame, in the direction of the vernal equinox and right ascension 0, and the nodal precession rate is relatively small (0.25 degrees/day). The LRS field of view covers a 12°-wide great-circle strip of the sky that passes near the north and south celestial poles, and right ascension 0 at the celestial equator. To change the strip of sky viewed by the LRS without changing the SIMV9 orbit and attitude values, catalog star unit vectors u_{ref} are offset in right ascension by α_{node}. This has the same effect on LRS observations as changing the ascending node of the orbit by $-\alpha_{\mathrm{node}}$.

Observation residuals are $\Delta y = h(u_{\mathrm{obs}}) - h(\hat{\mathbf{A}}_i^{\mathrm{LRS}}u_{\mathrm{ref}})$. All of the information needed for estimating deterministic corrections to the observations is contained in Δy and either $h(u_{\mathrm{obs}})$ or $h = (\hat{\mathbf{A}}_i^{\mathrm{LRS}}u_{\mathrm{ref}})$. Body frame residuals $\Delta y_{\mathrm{body}} = h[(\mathbf{A}_{\mathrm{ATLAS}}^{\mathrm{LRS}})^T h^{-1}(u_{\mathrm{obs}})] - h(\mathbf{A}_i^b u_{\mathrm{ref}})$ are useful for interpreting correlations in the residuals and alignments of multiple sensors, where $(\mathbf{A}_{\mathrm{ATLAS}}^{\mathrm{LRS}})^T h^{-1}(u_{\mathrm{obs}})$ and $\mathbf{A}_i^b u_{\mathrm{ref}}$ are expressed in a local frame based on the body frame x-axis with $\mathbf{i} = [1 \quad 0 \quad 0]^T \times \mathbf{A}_i^b u_{\mathrm{ref}}$, $\mathbf{j} = \mathbf{k} \times \mathbf{i}$, and $\mathbf{k} = \mathbf{A}_i^b u_{\mathrm{ref}}$. Celestial frame residuals $\Delta y_{\mathrm{ICRF}} = h[(\mathbf{A}_{\mathrm{ATLAS}}^{\mathrm{LRS}}\mathbf{A}_i^b)^T h^{-1}(u_{\mathrm{obs}})] - h(u_{\mathrm{ref}})$ from multiple passes of a particular star provide information for improving its mission catalog record, where $(\mathbf{A}_{\mathrm{ATLAS}}^{\mathrm{LRS}}\mathbf{A}_i^b)^T h^{-1}(u_{\mathrm{obs}})$ and u_{ref} are expressed in a local frame based on the celestial frame $\mathbf{z}$-axis with $\mathbf{i} = [0 \quad 0 \quad 1]^T \times u_{\mathrm{ref}}$, $\mathbf{j} = \mathbf{k} \times \mathbf{i}$, and $\mathbf{k} = u_{\mathrm{ref}}$.

The observation sensitivity matrix representing the relationship of star observations to filter states is

$$\mathbf{H} = \frac{\partial y}{\partial x} = \frac{\partial h}{\partial u}\frac{\partial u}{\partial x} = \frac{\partial h}{\partial u}\left[\frac{\partial u}{\partial a} \quad \mathbf{0} \quad \frac{\partial u}{\partial a_{\mathrm{LRS}}}\right] \qquad (10)$$

where from $h(u) = [u_1/u_3 \quad u_{2/u_3}]^T$

$$\frac{\partial h}{\partial u} = \begin{bmatrix} 1/u_3 & 0 & -u_1/u_3^2 \\ 0 & 1/u_3 & -u_2/u_3^2 \end{bmatrix} \qquad (11)$$

The factors $\partial u/\partial a$ and $\partial u/\partial a_{\mathrm{LRS}}$ represent the sensitivity of star observations to ATLAS attitude and LRS alignment variations. Their derivation here follows [6,7].

For $\partial u/\partial a$ the alignment is held constant and absorbed in $\mathbf{A}_{\mathrm{ATLAS}}^{\mathrm{LRS}}$. For a reference attitude $\mathbf{A}_i^r(t)$ arbitrarily close to $\mathbf{A}_i^{\mathrm{ATLAS}}(t)$ and a small attitude error rotation vector a with the first-order approximation $\mathbf{A}(a) \approx (\mathbf{I} - [a\times])$, the attitude is modeled as $\mathbf{A}_i^{\mathrm{ATLAS}}(t) = (\mathbf{I} - [a\times])\mathbf{A}_i^r(t)$. Observed and reference unit vectors are related by $u = \mathbf{A}_{\mathrm{ATLAS}}^{\mathrm{LRS}}\mathbf{A}_i^{\mathrm{ATLAS}}(t)u_{\mathrm{ref}}$ and for $a_i^r \to a_i^{\mathrm{ATLAS}}$ as $a \to 0$

$$u = \mathbf{A}_{\mathrm{ATLAS}}^{\mathrm{LRS}}\mathbf{A}_i^r(t)u_{\mathrm{ref}} - \mathbf{A}_{\mathrm{ATLAS}}^{\mathrm{LRS}}[a\times]\mathbf{A}_i^r(t)u_{\mathrm{ref}} \qquad (12)$$

$$u = \mathbf{A}_{\mathrm{ATLAS}}^{\mathrm{LRS}}\mathbf{A}_i^r(t)u_{\mathrm{ref}} - \mathbf{A}_{\mathrm{ATLAS}}^{\mathrm{LRS}}[\mathbf{A}_i^r(t)u_{\mathrm{ref}}\times]a \qquad (13)$$

$$\partial u/\partial a = \mathbf{A}_{\mathrm{ATLAS}}^{\mathrm{LRS}}[\mathbf{A}_i^{\mathrm{ATLAS}}(t)u_{\mathrm{ref}}\times] \qquad (14)$$

Similarly, for $\partial u/\partial a_{\mathrm{LRS}}$ with a reference alignment $\mathbf{A}_b^r$ arbitrarily close to $\mathbf{A}_{\mathrm{ATLAS}}^{\mathrm{LRS}}$ and the approximation $\mathbf{A}(a_{\mathrm{LRS}}) \approx (\mathbf{I} - [a_{\mathrm{LRS}}\times])$, the LRS alignment is modeled as $\mathbf{A}(a_{\mathrm{LRS}})\mathbf{A}_{\mathrm{ATLAS}}^r = (\mathbf{I} - [a_{\mathrm{LRS}}\times])\mathbf{A}_{\mathrm{LRS}}^r$. Observed and reference unit vectors are related by $u = \mathbf{A}(a_{\mathrm{LRS}})\mathbf{A}_{\mathrm{ATLAS}}^r\mathbf{A}_i^{\mathrm{ATLAS}}(t)u_{\mathrm{ref}}$ and

$$u = \mathbf{A}_{\mathrm{ATLAS}}^r\mathbf{A}_i^{\mathrm{ATLAS}}(t)u_{\mathrm{ref}} - [a_{\mathrm{LRS}}\times]\mathbf{A}_{\mathrm{ATLAS}}^r\mathbf{A}_i^{\mathrm{ATLAS}}(t)u_{\mathrm{ref}} \quad (15)$$

$$u = \mathbf{A}_{\mathrm{ATLAS}}^r\mathbf{A}_i^{\mathrm{ATLAS}}(t)u_{\mathrm{ref}} + [\mathbf{A}_{\mathrm{ATLAS}}^r\mathbf{A}_i^{\mathrm{ATLAS}}(t)u_{\mathrm{ref}}\times]a_{\mathrm{LRS}} \quad (16)$$

$$\partial u/\partial a_{\mathrm{LRS}} = [\mathbf{A}_{\mathrm{ATLAS}}^j\mathbf{A}_i^{\mathrm{ATLAS}}(t)u_{\mathrm{ref}}\times] \qquad (17)$$

Alignment updates are performed using the Kalman gain $\mathbf{K} = \mathbf{P}\mathbf{H}^T(\mathbf{H}\mathbf{P}\mathbf{H}^T + \mathbf{R})^{-1}$, estimated state correction $\Delta x = [\Delta a^T \quad \Delta b^T \quad \Delta a_{\mathrm{LRS}}^T] = \mathbf{K}\Delta y$, and covariance update $\mathbf{P}_+ = (\mathbf{I} - \mathbf{K}\mathbf{H})\mathbf{P}_-$. The rate bias update is $\hat{b}_+ = \hat{b}_- + \Delta b$, the updated attitude estimate is $q_{b+} = q(\Delta a) \otimes q_{b-}$, and the updated LRS alignment is $a_{\mathrm{LRS}+} = a_{\mathrm{LRS}-} + \Delta a_{\mathrm{LRS}}$.

B. Alignment Process Noise

The alignment process noise σ_{LRS} in Eq. (7) is the tuning parameter for alignment tracking and depends on the characteristics of the star observations and the LRS motion. More LRS motion means higher σ_{LRS} value, but as σ_{LRS} increases alignment tracking becomes more sensitive to noise and other errors in the star observations. The objective is to find an adequate σ_{LRS} for reacting to LRS motion and not reacting to star observation issues and errors. As a corollary, different star observation characteristics, in particular different LRS sensitivities, mean different σ_{LRS} values.

Multiple-model adaptive estimation is used to estimate σ_{LRS} by testing a set of candidates. Each candidate is implemented in its own filter H_i and the set of candidates form a filter bank $H_i; i = 1, \ldots, n$. Simulated observations are input to the filter bank, and the results are compared with simulation truth to select the best candidate. The description here follows [27–29]. The observation probability for a candidate and filter bank member H_i is given by $\mathbf{P}(y_k|H_i) = (2\pi)^{-m/2}|\mathbf{S}_k|^{-1/2}\exp(-\Delta y_k^T\mathbf{S}_k^{-1}\Delta y_k/2)$, where $\mathbf{S}_k = \mathbf{H}_k\mathbf{P}_k\mathbf{H}_k^T + \mathbf{R}_k$ and m is the number of filter states. At the beginning of a simulation, each of the H_i is assigned the same probability $P_0(H_i) = n^{-1}$ of being the best. The probabilities are updated by $P_k(H_i) = P(y_k|H_i)P_{k-1}(H_i)/\sum_{j=1}^n P(y_k|H_j)P_{k-1}(H_j)$. If a $P_k(H_i)$ approaches 1 as t_k increases, it is evidence that the associated filter H_i and candidate are the most correct.

Table 1 shows the resulting estimated σ_{LRS} values for three LRS sensitivities and four LRS motion amplitudes. The sensitivity values

Table 1 Estimated σ_{LRS}, arcsec/s$^{1/2}$

LRS sensitivity, instrument magnitudes	LRS motion amplitude, arcsec			
	1	2	5	10
4.8	0.015	0.023	0.040	0.061
5.0	0.013	0.022	0.038	0.058
5.2	0.012	0.019	0.035	0.057

4.8, 5.0, and 5.2 are unitless ratios expressing limiting magnitude cutoff, as described in Eq. (9). LRS motion is modeled as a simple sinusoidal $a \sin \theta$, and the amplitudes $a = 1, 2, 5, 10$ arcsec are half of the peak-to-peak amplitudes.

Table 1 demonstrates a strong dependence of σ_{LRS} on LRS motion, and a weak but detectable dependence on LRS sensitivity over this range of input values.

C. Simulated LRS Alignment Variations

LRS alignment variation is expected to be periodic motion repeating with the orbital period of 5670 s. Deviations from the orbital variation due to scan maneuvers are expected to be small but are a significant question for specialized studies. Evolution of the orbital variation is expected on time scales of days and weeks as the beta angle changes.

Two LRS motion cases are used here for Monte Carlo simulation: a baseline sinusoidal motion, and ICESat-1 flight data. The baseline case includes a random initial phase so that the motion peaks at different times in each simulation run. Over a large set of runs there will be peaks at or near every part of the orbit. The randomly distributed sinusoidal motions build up a map of performance characteristics with respect to the sky (numbers of stars, alignment tracking errors, etc.) and provide increasingly uniform coverage as the number of simulation runs increase. The baseline sinusoid amplitude is 5 arcsec (10 arcsec peak-to-peak).

ICESat-1 flight data include directly observed alignment variations that are used here as the basis for a class of realistic nonsinusoidal models [1,16,30]. On ICESat-1, the alignment between the LRS and instrument star tracker was directly observed by the LRS while a reference signal linking the LRS and IST coordinate frames was operating [1]. Figure 8 shows LRS observations of the reference signal motion over one orbit.

The orbital period is scaled from 5790 s for ICESat-1 to 5670 s for ICESat-2. Because it provides a clear reference point, the jump or step-change due to entering sunlight is used to define $t = 0$ within the simulated orbital variation. In practice, the jump comes at the same phase of successive orbits, but again a random initial phase is used in each simulation run so that the jumps occur throughout the orbit, as for the baseline case.

The two alignment cases are viewed as test signals that are input to the processor in order to study the output response. This is particularly true for the sharp jump in the ICESat-1 case, because it approximates a step function. It is treated as a proxy for an impulse

function for the purposes of driving a range of processor responses and alignment tracking errors.

D. Alignment Tracking Error

LRS alignment tracking error is a time series of rotation vector differences $\boldsymbol{e}(t_k) = \hat{\boldsymbol{a}}_{\text{LRS}}(t_k) - \boldsymbol{a}_{\text{LRS}}(t_k)$ between the estimated alignment $\hat{\boldsymbol{a}}_{\text{LRS}}$ and the simulation truth $\boldsymbol{a}_{\text{LRS}}$. Using the LRS coordinate frame conventions from Fig. 1, the error rotation is expressed in LRS frame roll, pitch, and yaw $\boldsymbol{e} = [\,e_x \quad e_y \quad e_z\,]$. The LRS frame z axis is zenith pointing, while ATLAS and body frame z axes are nadir pointing, and expressed in the body frame $\boldsymbol{e} = [\,e_{bx} \quad -e_{by} \quad -e_{bz}\,]$. As discussed in Sec. III.A, the focus here is on roll errors $e_k \equiv e_x(t_k)$. Roll and pitch results are similar in principle, and the yaw results are on a much larger scale because the star observations are significantly less sensitive to yaw than to roll and pitch.

A set of $i = 1, \ldots, n$ runs are performed for every Monte Carlo simulation case, with n normally 50 here. The roll error time series for each run $e_k(i)$ is sampled at 10 s intervals $j = 1, \ldots, m$. Within each 10 s sample $e_k(i, j)$, there are $k = 1, \ldots, 100$ roll error values, matching the 10 Hz observation frequency. The mean $\mu(i, j) \equiv \sum_{k=1}^{100} e_k(i, j)/100$ and squared rms $\text{rms}(i, j)^2 \equiv \sum_{k=1}^{100} e_k(i, j)^2/100$ are computed for each sample. The standard deviation $\sigma(i, j)^2 = \text{rms}(i, j)^2 - \mu(i, j)^2$ is computed as needed. This approach is directed toward computing overall results for sample j from all n Monte Carlo runs. Mean, rms, and standard deviation values for sample j are given by

$$\mu(j) = \sum_{i=1}^{n} \mu(i, j)/n \tag{18}$$

$$\text{rms}(j)^2 = \sum_{i=1}^{n} \text{rms}(i, j)^2/n \tag{19}$$

$$\sigma(j)^2 = \text{rms}(j)^2 - \mu(j)^2 \tag{20}$$

Results for all samples and all runs are given by

$$\mu = \sum_{j=1}^{m} \sum_{i=1}^{n} \mu(i, j)/mn \tag{21}$$

$$\text{rms}^2 = \sum_{j=1}^{m} \sum_{i=1}^{n} \text{rms}(i, j)^2/mn \tag{22}$$

$$\sigma^2 = \text{rms}^2 - \mu^2 \tag{23}$$

Time series of $\text{rms}(j)$ values for n runs are a useful performance measure as demonstrated in Figs. 9–11 over a 5670 s orbital period ($j = 1, \ldots, 567$). The Monte Carlo simulation overall case here is
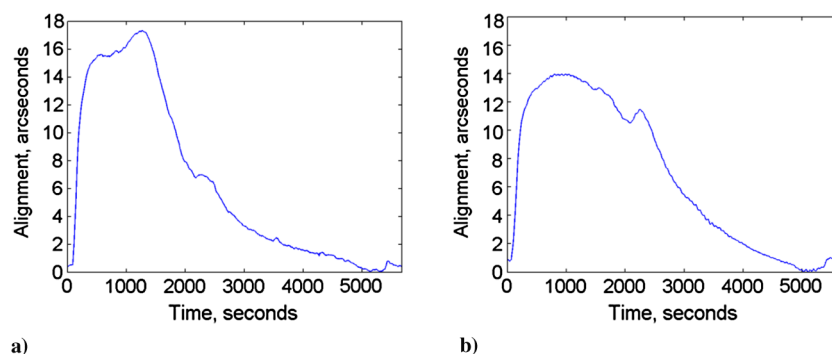

a)

b)

Fig. 8 ICESat-1 flight data for LRS alignment orbital variation in a) roll and b) pitch.
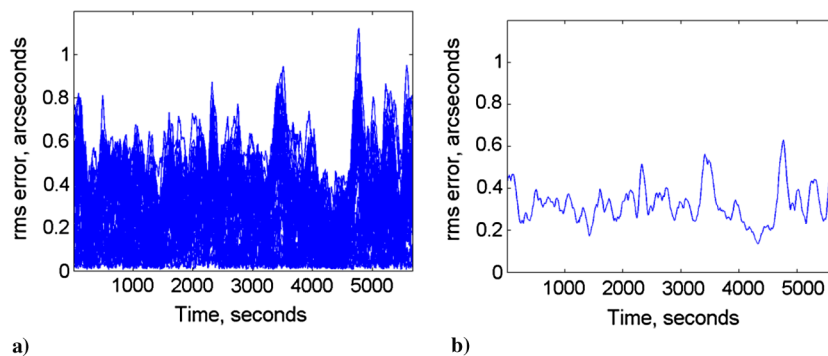
Fig. 9   Roll rms errors for a) each of 50 runs and b) all 50 runs together.
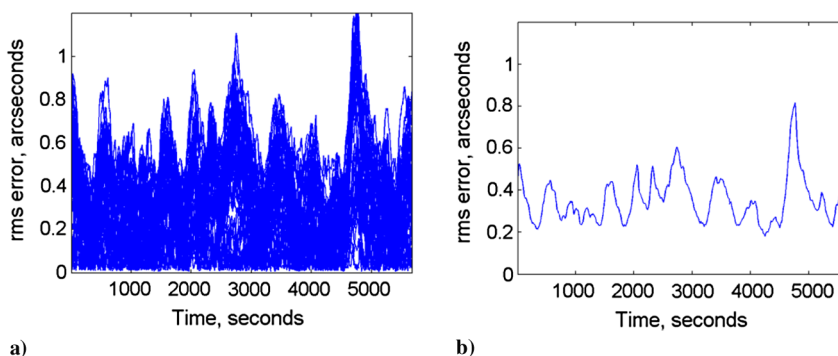

Fig. 10   Pitch rms errors for a) each of 50 runs and b) all 50 runs together.
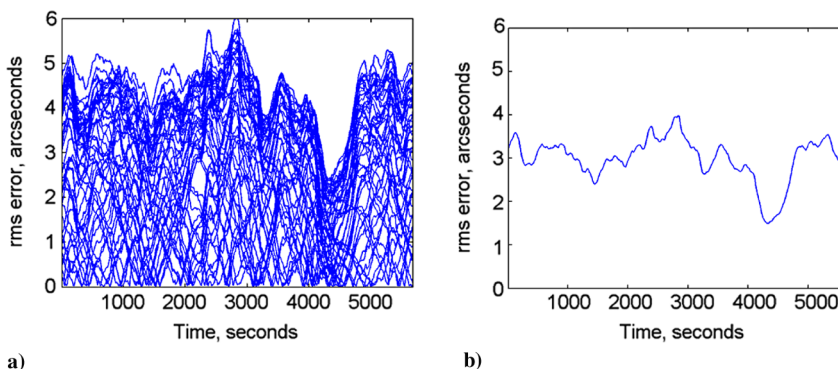

Fig. 11   Yaw rms errors for a) each of 50 runs and b) all 50 runs together.

the baseline sinusoidal alignment variation and LRS sensitivity 5.2. The plots on the left show $\mathrm{rms}(i, j)$ for all $n = 50$ runs, and the plots on the right show $\mathrm{rms}(j)$. Figures 9–11 show roll, pitch, and yaw, respectively, to demonstrate the similarity of roll and pitch and the difference of yaw. The overall rms values calculated using Eq. (22) are roll 0.34 arcsec, pitch 0.37 arcsec, and yaw 3.04 arcsec.

The broad distributions of results in the left-hand plots of $\mathrm{rms}(i, j)$ reflect the random phases of the baseline sinusoidal alignment variations, making that the results in each of the 50 runs differ significantly. The right-hand plots of $\mathrm{rms}(j)$ are cumulative results that reduce the effects of individual runs. In the limit as n grows very large, the $\mathrm{rms}(j)$ plots show results that are effectively independent of individual runs.

E.   Star Observations and Alignment Tracking

Two features are apparent in Figs. 9–11. Beginning at 4000 s the tracking errors decrease, followed immediately by an increase before 5000 s. Figure 12 shows the numbers of observed stars. The drop
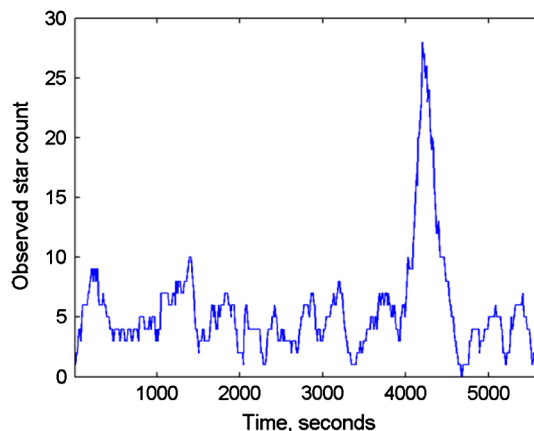

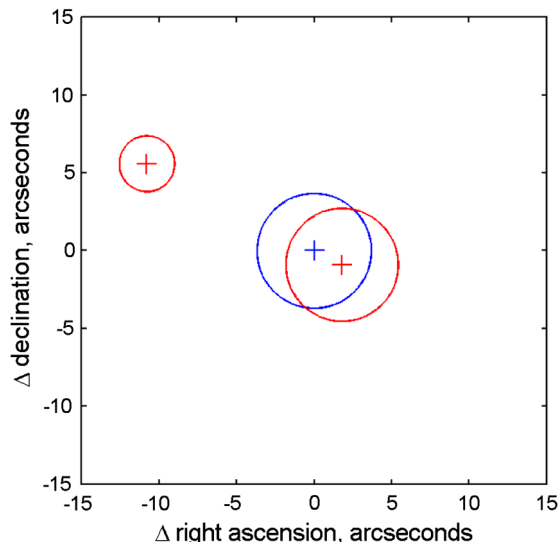**Fig. 12   Star counts for LRS sensitivity 5.2.**

Fig. 13   Near-neighbor star Skymap 7080327.

corresponds to a peak in the number of observed stars as the LRS line of sight passes through the Milky Way, and the increase corresponds to a star gap in which counts drop to 0 or 1. LRS sensitivity is 5.2 in this simulation. For lower sensitivities, the star peak is smaller and the star gap is larger.

Figures 9–12 demonstrate the significance of observed star counts and therefore of LRS sensitivity. Star counts can be predicted using a star catalog and a model of LRS sensitivity; however, star counts alone provide no information about alignment and attitude tracking performance. Monte Carlo simulation simultaneously provides information about tracking performance (Figs. 9–11) and star counts (Fig. 12). It also provides detailed information about special cases such as long star gaps and the conditions under which near-neighbor stars are observed. Star gaps are directly characterized by the rms tracking error time series. Over many simulation runs, the randomly phased alignment variations act as test signals that produce output signals during the gaps. An analogy is searching for holes on a surface: searching point by point is similar to using a star catalog; putting a light behind the surface is similar to using tracking errors.

Near-neighbor stars are cases where the mission catalog record is a center of light prediction for two or more real stars. Figure 13 shows a case that is important in the results section. The predicted center of light is at the origin, Skymap 7080327 is bright and near the center of light, and Skymap 7080200 is to the upper left. The radii of the circles are scaled to represent predicted instrument magnitude for the center of light and visual magnitude for the stars. Near-neighbors are identified here by the brightest member, and so, for example, the case shown in Fig. 13 is referred to as Skymap 7080327.

Near-neighbor stars are potential bad stars [23,25,26]. Center of light prediction depends on the LRS sensitivity and response to the brightness and color of each member star, as well as spatial geometry [24]. The detailed conditions in which a near-neighbor star is observed are also significant. If 20 stars are being observed, a small error in the center of light prediction for 1 near-neighbor star has little effect on the filter. If the near-neighbor star is the only star being observed, an error in the center of light prediction can propagate directly into the state estimate, as demonstrated below.

V.   Results for LRS Pointing Knowledge Performance

The overall uncertainty in LRS pointing knowledge is approximated by $\sigma_{LRS}^2 = \sigma_{ATLAS}^2 + \sigma_{LRSA}^2$, where σ_{ATLAS} is reference platform attitude uncertainty and σ_{LRSA} is LRS alignment tracking uncertainty. LRS pointing refers here to roll, pitch, and the direction of the LRS line of sight in the celestial frame.

Results for rms attitude tracking errors are shown in Table 2 and are used as an estimate of σ_{ATLAS}.

A reference platform attitude uncertainty of $\sigma_{ATLAS} = 0.06$ arcsec is adopted here as a baseline reference value.

Results for σ_{LRSA} are based on a set of Monte Carlo simulations in which the LRS views the full sky. The orbit inclination of 94° means that the great-circle strip of sky observed by the LRS always includes the north and south celestial poles. Varying the right ascension of the ascending node α from 0° to 180° in 10° steps $\alpha = 0°, 10°, \ldots, 170°$ gives full sky coverage, with the ascending passes sweeping over half of the sky and the descending passes sweeping over the other half. Many of the results discussed here are for these 18 orbits, often with the addition of $\alpha = 180°$ for comparison with $\alpha = 0°$ and verification of periodic patterns in the results.

These results are for random phasing of the LRS motion during the simulation runs. The random phasing in effect puts equal weight on each region of the sky. This normalizes the results for comparison, but means that they are a type of upper-bound uncertainty estimate. In flight telemetry, the phasing of the LRS motion is approximately constant from one orbit to the next, not random, and there are normally adequate LRS star observations during rapid changes of alignment. The Monte Carlo results tend to find the worst cases, with rapid LRS motion and no star observations, more frequently than they occur in flight data. This is particularly true for the ICESat-1 flight data case. The asymmetric and sharp nature of its saw-tooth motion (Fig. 8) picks out areas of the sky with sparse star observations more strongly than the symmetric and smooth baseline motion case.

Figure 14 summarizes roll axis results for the baseline LRS motion case. The left plot shows the number of star observations per orbit as a function of α and LRS sensitivity. The number of star observations is smallest for orbits near $\alpha = 0°$ and largest near $\alpha = 90°$. The right plot shows median$[\sigma(j)]$ [Eq. (20)] for roll over 50 simulation runs at each α and LRS sensitivity. The expected inverse relationship between sensitivity in the left plot and tracking performance in the right plot is clear.

Figure 15 shows overall rms [Eq. (22)] for roll over the same 50 runs as Fig. 14. The values in Fig. 15 are correlated with the median$[\sigma(j)]$ values in Fig. 14 because the errors are approximately zero mean with rms$(j) \approx \sigma(j)$. However, the rms values are more sensitive to certain events than the median$[\sigma(j)]$ values. The spike at $\alpha = 80°$ is discussed in more detail below.

Table 3 gives the rms LRS roll tracking errors for both LRS motion cases and the three LRS sensitivities, with the baseline motion case to the left and the ICESat-1 flight data case to the right. As in Fig. 15, each rms is computed from $50 \times 5670 \times 10 = 2.8 \times 10^6$ error values.

Table 4 characterizes overall LRS pointing knowledge uncertainty. It shows LRS pointing uncertainties $\sigma_{LRS} = (\sigma_{ATLAS}^2 + \sigma_{LRSA}^2)^{1/2}$ for the three LRS sensitivities, both motion cases, and three scalings (0.5, 1, 1.5) of the motion amplitudes.

A pointing knowledge uncertainty of $\sigma_{LRS} = 0.27$ arcsec is adopted here as a baseline reference value.

A.   Sky Maps

The estimate $\sigma_{LRS} = 0.27$ arcsec characterizes performance over the full sky. Local performance varies significantly, particularly in regions where there are fewer stars than normal. The rms roll tracking error in Fig. 15 demonstrates a significant localized interaction between the star observations and alignment tracking errors in the spike at $\alpha = 80°$.

Figure 16 shows star count and rms roll tracking error time series for the orbit at $\alpha = 80°$. The 50 Monte Carlo runs use the baseline LRS motion case. The gap in star observations and resulting spike in

Table 2   Reference platform rms attitude tracking errors, arcsec

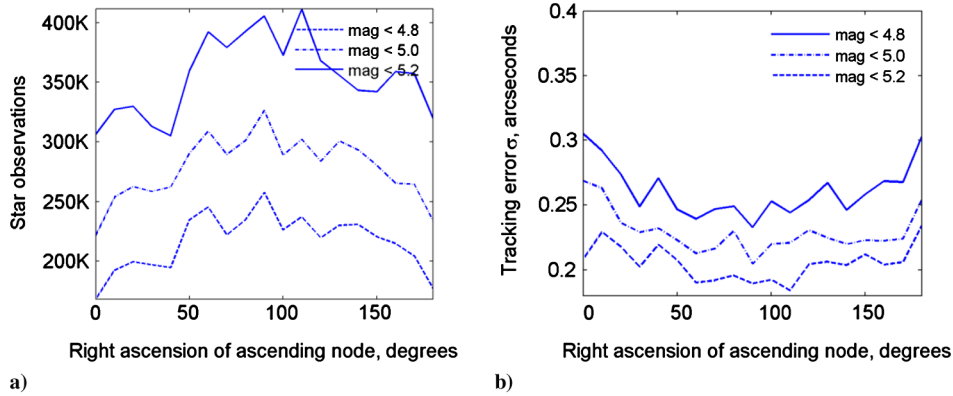| Noise scaling	Nadir pointing	Peak acceleration
0.33	0.03	0.03
0.5	0.04	0.04
1	0.06	0.05
2	0.1	0.08
3	0.15	0.13

Fig. 14 Relationship of a) LRS sensitivity and b) roll tracking error $\mathrm{median}(\sigma(j))$.
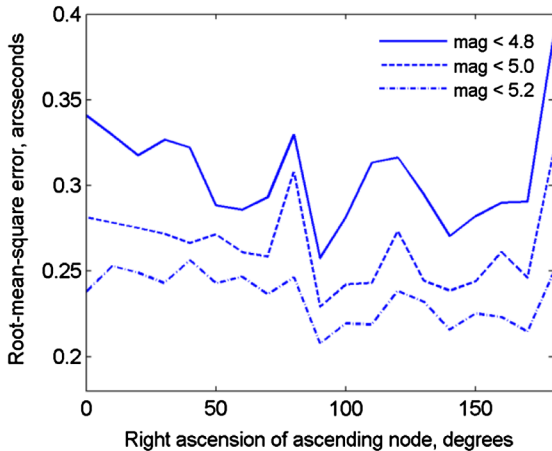

Fig. 15 The rms roll tracking error.

tracking errors near 4800 s is the source of the upward spike in Fig. 15. The results for the three LRS sensitivity cases 4.8, 5.0, and 5.2 are plotted together as three time series. The time series with fewer star observations and larger tracking errors is the sensitivity 4.8 case.

These time series represent a one-dimensional slice or sample of the full sky. If they are laid vertically side by side with similar time

series for other ascending nodes, two-dimensional maps of the sky are built up, with the ascending node on the horizontal axis and time on the vertical axis. These sky maps are generated here by performing 50 Monte Carlo runs at each integer orbit node from 0° to 359°, with 10 s subsampling of each run. The resulting maps consist of a grid of 567×360 cells. The results from 180° to 359° are mostly redundant with the results from 0° to 179°, but there are small geometric differences between ascending and descending passes in a given region of the sky.

Figures 17–19 show star observation counts and rms roll tracking errors for the baseline LRS motion case and LRS sensitivities 4.8, 5.0, and 5.2. Results for each integer node from 0° to 180° are plotted. Node number forms the horizontal axis, from node 0° at the origin to node 180° on the right. The vertical axis is time with $t = 0$ s at the origin and 5670 s at the top. At a given node, ascending from the horizontal axis to the top of the plot traverses the same type of time series as in Fig. 16. The spacecraft is passing through the ascending node at $t = 0$ s and the horizontal axis corresponds to declination 0°. At the top of the plot the spacecraft has returned to declination 0° by completing an orbit after passing the North Pole at $t = 1417$ s, the descending node at $t = 2834$ s, and the South Pole at $t = 4251$ s.

The $567 \times 360 = 204,120$ cells of the sky maps are used to characterize the overall abundances of star gaps and near-neighbor stars. Each cell represents 10 s of time and the cells are all equivalent for the purposes of determining how much time the LRS spends in star gaps or observing near-neighbor stars, despite the variable spatial overlap of adjacent cells. The cells have more spatial overlap on the sky at the celestial poles and less overlap at the celestial equator. Near the poles the cells from every orbit cover the same small region of the sky; they are similar to a set of rotated but essentially overlapping LRS fields of view. Table 5 shows overall characteristics of the sky for the three LRS sensitivities.

Cells containing only a near-neighbor star are relatively rare and dominated by a handful of near-neighbors. This is significant because these are cases where biased center-of-light position predictions and bad stars are most problematic. In other words, only a handful of near-neighbor stars are potentially significant problems. Important examples are shown in Table 6. Near-neighbor stars are identified here by the Skymap number of the brightest member star.

Table 3 The rms roll tracking error, arcsec

Node	Baseline			ICESat-1		
	4.8	5	5.2	4.8	5	5.2
0	0.34	0.28	0.24	0.40	0.34	0.29
10	0.33	0.28	0.25	0.40	0.33	0.31
20	0.32	0.28	0.25	0.36	0.33	0.31
30	0.33	0.27	0.24	0.40	0.32	0.32
40	0.32	0.27	0.26	0.40	0.32	0.31
50	0.29	0.27	0.24	0.34	0.32	0.28
60	0.29	0.26	0.25	0.36	0.32	0.27
70	0.29	0.26	0.24	0.38	0.33	0.28
80	0.33	0.31	0.25	0.38	0.35	0.34
90	0.26	0.23	0.21	0.30	0.27	0.26
100	0.28	0.24	0.22	0.33	0.30	0.28
110	0.31	0.24	0.22	0.38	0.30	0.26
120	0.32	0.27	0.24	0.38	0.32	0.29
130	0.29	0.24	0.23	0.35	0.30	0.32
140	0.27	0.24	0.22	0.32	0.28	0.27
150	0.28	0.24	0.23	0.33	0.31	0.28
160	0.29	0.26	0.22	0.36	0.33	0.26
170	0.29	0.25	0.21	0.34	0.30	0.26
180	0.39	0.32	0.25	0.42	0.39	0.30

Table 4 LRS pointing knowledge uncertainty $\sigma_{\mathrm{LRS}} = (\sigma_{\mathrm{ATLAS}}^2 + \sigma_{\mathrm{LRSA}}^2)^{1/2}$, arcsec

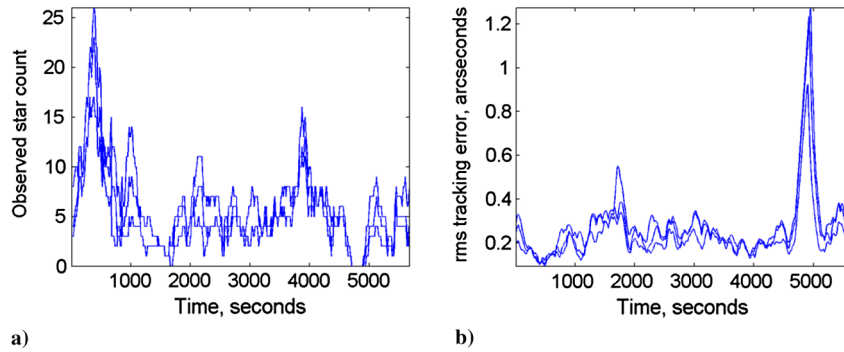| LRS motion	LRS sensitivity		
	4.8	5	5.2
Baseline × 0.5	0.15	0.13	0.12
Baseline × 1.0	0.31	0.27	0.24
Baseline × 1.5	0.41	0.35	0.33
ICESat-1 × 0.5	0.21	0.17	0.15
ICESat-1 × 1.0	0.36	0.32	0.29
ICESat-1 × 1.5	0.47	0.45	0.42

a)　　　　　　　　　　b)

Fig. 16　Node 80° a) star observation counts and b) rms roll tracking errors.
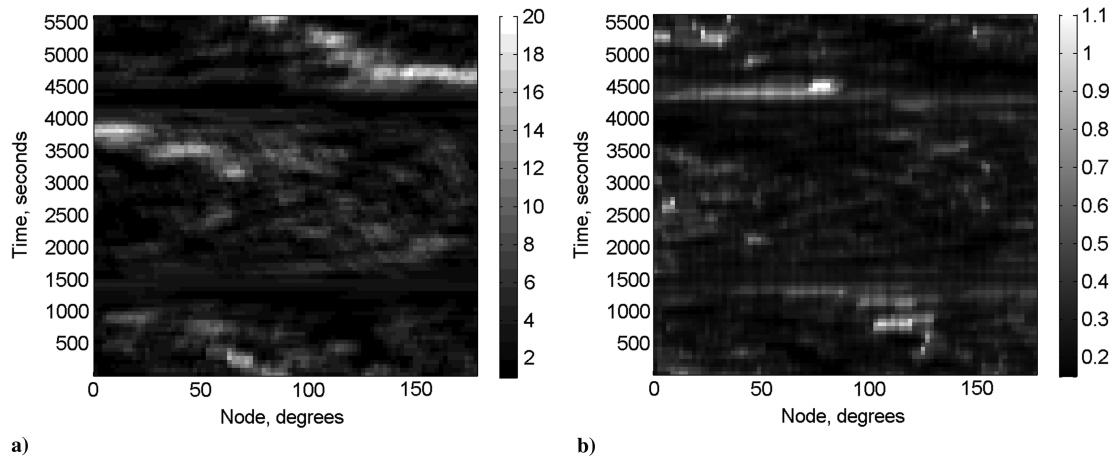

a)　　　　　　　　　　b)

Fig. 17　LRS sensitivity 4.8 a) star counts and b) rms roll tracking errors in arcseconds.
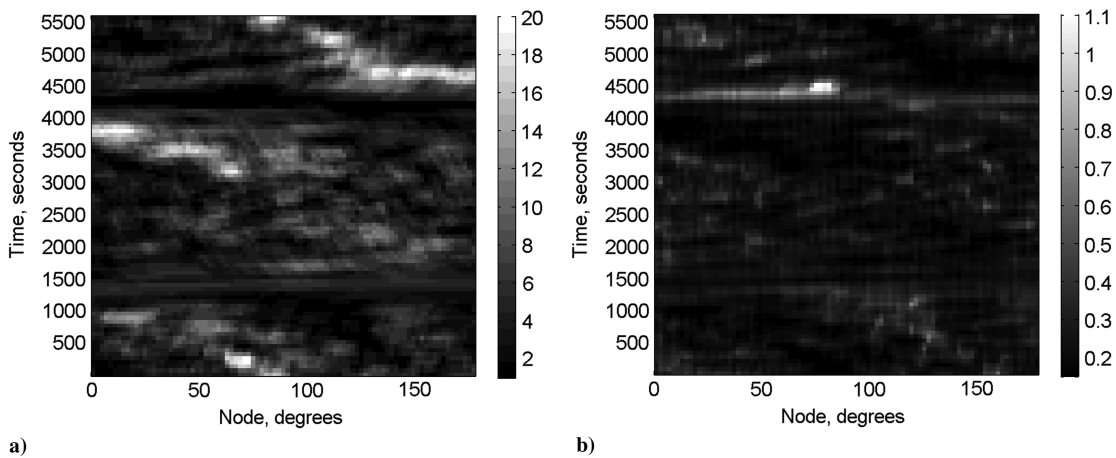

a)　　　　　　　　　　b)

Fig. 18　LRS sensitivity 5.0 a) star counts and b) rms roll tracking errors in arcseconds.
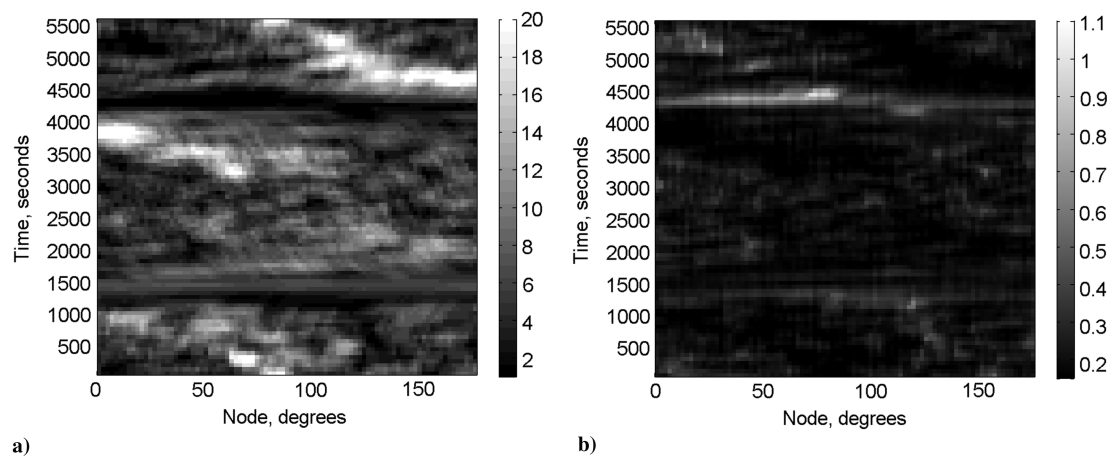

a)　　　　　　　　　　b)

Fig. 19　LRS sensitivity 5.2 a) star counts and b) rms roll tracking errors in arcseconds.

Table 5   Sky characteristics for maps with 204,120 cells

	Sensitivity		
	4.8	5.0	5.2
Number of unique stars	1,083	1,385	1,750
Number of unique near-neighbor stars	99	114	146
Cells with no stars	8,210	4,084	3,474
Percentage of cells with no stars	0.04	0.02	0.017
Cells with a near-neighbor star	53,214	61,632	78,666
Percentage of cells with near-neighbor stars	0.26	0.30	0.38
Cells containing only near-neighbor stars	918	481	246

Table 6   Counts of cells containing only a near-neighbor star

Sensitivity 4.8		Sensitivity 5.0		Sensitivity 5.2	
Skymap id	Cells	Skymap id	Cells	Skymap id	Cells
8460162	249	8460162	149	8460162	89
18560046	133	18560046	73	18560046	45
7080327	78	7080327	52	7080327	33
15340134	45	15340134	45	15340134	8
12560007	175	12560007	4	——	——
14410169	58	14410169	3	——	——
——	——	2590026	51	2590026	49
——	——	8120049	23	8120049	10

B.   Star Gaps and Bad Stars

The tracking error maps for all three LRS sensitivities (Figs. 17–19) have a significant feature in common: a peak near node 80° and $t = 4500$ s caused by a star gap at right ascension 88° and declination −80°. What makes this gap special is its length for orbits with nodes
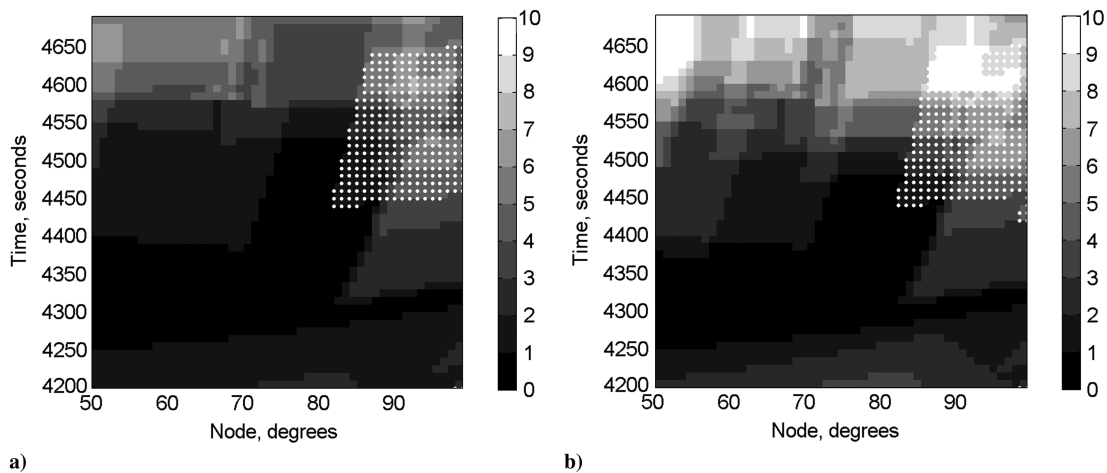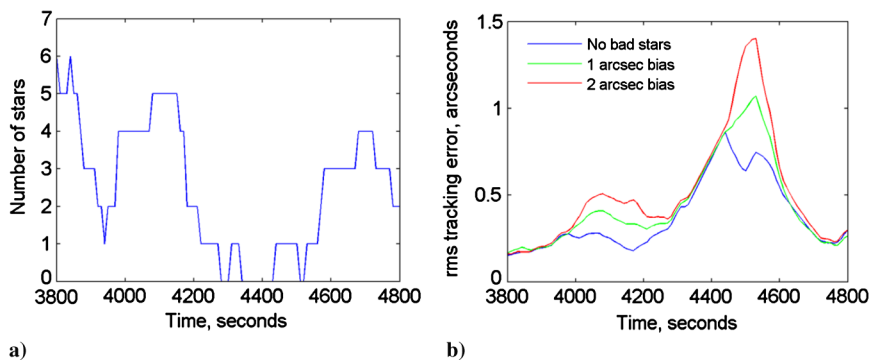
between approximately 75° and 85°. Figure 20 shows that, due to geometry, for these orbits the gap is approximately 250 s long. The shape of the gap in the sky happens to coincide with the direction that the spacecraft is traveling. Figure 20 also shows a dot pattern indicating where the LRS is observing the near-neighbor star Skymap 7080327. It is the only observable star as the spacecraft leaves the gap for nodes between approximately 80° and 85°.

High-resolution full-sky maps confirm that the situation in Fig. 20 is unusual because of both the size of the star gap and the adjacent isolated near-neighbor star. This situation is a good test case for studying the effects of both star gaps and problematic near-neighbor stars.

Figure 21 shows the effects of near-neighbor stars with biased center-of-light position predictions (bad stars) on rms alignment tracking error. The left plot in Fig. 21 shows the counts of observed stars near the star gap for orbit node 82° and LRS sensitivity 4.8. The star observed immediately after the main part of the gap, from 4340 to 4500 s, is the isolated near-neighbor star Skymap 7080327. Another near-neighbor star is observed shortly before the gap, from 3980 to 4170 s. The two near-neighbor stars are identified here by their brightest members: Skymap 7080327 and Skymap 16200091, respectively.

The right plot shows simulation results for three cases: a baseline case and two bad star cases. In the baseline case, both near-neighbor stars have unbiased center-of-light position predictions. In the two bad star cases, the center-of-light positions are both biased with a position offset of 1 or 2 arcsec. Each rms tracking error time series combines the results from 50 simulation runs.

Before the star gap, the effect of center-of-light bias for Skymap 16200091 is reduced by the filter updates from the other stars being observed simultaneously. In the star gap, however, the full effect of the bias for Skymap 7080327 is added to the previously accumulated effects of the gap.

Fig. 20   Expanded view of star gap for LRS sensitivities a) 4.8 and b) 5.2.

Fig. 21   Roll tracking error with bad stars near the star gap.

VI.   Conclusions

Pointing knowledge performance is strongly dependent on the sensitivity of the laser reference sensor (LRS) star observations. A decrease in sensitivity means more need for modeling of the LRS motion relative to the SSTs. Ideally, the motion model would provide adequate pointing knowledge performance by itself and the star observations would act as empirical verification. In practice, star observations are used to correct and improve the motion model over time, and if they are plentiful enough, the model becomes less necessary.

The results for the ICESat-1 flight data case demonstrate that, if there is rapid LRS motion, ground processing to learn and model the characteristics of the motion will be essential. Over time, ground processing can determine common features and trends in the motion and take advantage of that knowledge to improve the overall results.

Acknowledgment

References

[1] Smith, N., Bae, S., Webb, C., and Schutz, B. E., "Laser Reference Sensor Alignment Estimation from Reference Signal Observations," *Journal of Spacecraft and Rockets*, Vol. 51, No. 1, 2014, pp. 48–56.
doi:10.2514/1.A32546

[2] Smith, N., Bae, S., and Schutz, B. E., "Laser Reference Sensor Alignment Estimation from Star Observations," *Journal of Spacecraft and Rockets* (to be published).
doi:10.2514/1.A32669

[3] Smith, N., Bae, S., and Schutz, B. E., "ICESat-2 Precision Pointing Determination Algorithm Theoretical Basis Document," Report ICESat-2-SIPS-SPEC-1595, Center for Space Research, Austin, TX, 2013.

[4] Bae, S., Smith, N., and Schutz, B. E., "ICESat-1 Precision Pointing Determination Algorithm Theoretical Basis Document," NASA Rept. TM-2012-208641, Center for Space Research, Austin, TX, 2012.

[5] Pittelkau, M. E., "Survey of Calibration Algorithms for Spacecraft Attitude Sensors and Gyros," *AAS Astrodynamics Specialist Conference, Advances in the Astronautical Sciences*, Vol. 129, Univelt, San Diego, CA, 2007, pp. 651–706; also AAS Paper 2007-295.

[6] Pittelkau, M. E., "Kalman Filtering for Spacecraft System Alignment Calibration," *Journal of Guidance, Control, and Dynamics*, Vol. 24, No. 6, 2001, pp. 1187–1195.
doi:10.2514/2.4834

[7] Pittelkau, M. E., "Everything Is Relative in Spacecraft System Alignment Calibration," *Journal of Spacecraft and Rockets*, Vol. 39, No. 3, 2002, pp. 460–466.
doi:10.2514/2.3830

[8] Bayard, D. S., "An Overview of the Pointing Control System for NASA's Space Infra-Red Telescope Facility (SIRTF)," *AIAA Guidance, Navigation, and Control Conference*, AIAA 2003-5832, 2003.

[9] Bayard, D. S., and Kang, B. H., "A High-Order Kalman Filter for Focal Plane Calibration of NASA's Space Infrared Telescope Facility (SIRTF)," *AIAA Guidance, Navigation, and Control Conference*, AIAA Paper 2003-5824, 2003.

[10] Li, R., Needelman, D., Fowell, R., Tsao, T.-C., and Wu, Y.-W., "Reusable Stellar Inertial Attitude Determination (SIAD) Design For Spacecraft Guidance, Navigation & Control," *AIAA Guidance, Navigation, and Control Conference*, AIAA 2005-5928, 2005.

[11] Brenner, A. C., DiMarzio, J. P., and Zwally, H. J., "Precision and Accuracy of Satellite Radar and Laser Altimeter Data over the Continental Ice Sheets," *IEEE Transactions on Geosciences and Remote Sensing*, Vol. 45, No. 2, 2007, pp. 321–331.
doi:10.1109/TGRS.2006.887172

[12] Luthcke, S. B., Rowlands, D. D., McCarthy, J. J., Pavlis, D. E., and Stoneking, E., "Spaceborne Laser-Altimeter-Pointing Bias Calibration from Range Residual Analysis," *Journal of Spacecraft and Rockets*, Vol. 37, No. 3, 2000, pp. 374–384.
doi:10.2514/2.3571

[13] Luthcke, S. B., Carabajal, C. C., and Rowlands, D. D., "Enhanced Geolocation of Spaceborne Laser Altimeter Surface Returns: Parameter Calibration from the Simultaneous Reduction of Altimeter Range and Navigation Tracking Data," *Journal of Geodynamics*, Vol. 34, No. 3,

2002, pp. 447–475.
doi:10.1016/S0264-3707(02)00047-9

[14] Zwally, H. J., Schutz, B. E., Bentley, J., Bufton, T., Herring, J., Minster, J., Spinhirne, J., and Thomas, R., *GLAS/ICESat L1A Global Laser Pointing Data V031 [Digital Media]*, National Snow and Ice Data Center, Boulder, CO, 2003.

[15] Bae, S., and Schutz, B. E., "Precision Attitude Determination Using Gyro and Star Tracker Data with a Batch Least Squares Estimator," *AAS/AIAA Astrodynamics Conference, Advances in the Astronautical Sciences*, Vol. 123, Univelt, San Diego, CA, 2005, pp. 175–182; also AAS Paper 2005-260.

[16] Bae, S., Webb, C., and Schutz, B. E., "Star Tracker Misalignment Calibration for the ICESat Mission," *AAS/AIAA Space Flight Mechanics, Advances in the Astronautical Sciences*, Vol. 124, Univelt, San Diego, CA, 2006, pp. 113–124; also AAS Paper 2006-107.

[17] Sirota, J. M., Bae, S., Millar, P., Mostofi, D., Webb, C., Schutz, B., and Luthcke, S., "The Transmitter Pointing Determination in the Geoscience Laser Altimeter System," *Geophysical Research Letters*, Vol. 32, No. 22, 2005, pp. 1–4.
doi:10.1029/2005GL024005

[18] Bae, S., Magruder, L., Ricklefs, R., Webb, C., Yoon, S., and Schutz, B. E., "ICESat/GLAS Precision Attitude Determination for Early Laser Operation," *AAS/AIAA Space Flight Mechanics Meeting, Advances in the Astronautical Sciences*, Vol. 124, Univelt, San Diego, CA, 2004; also AAS Paper 2004-118.

[19] Bae, S., Webb, C., and Schutz, B. E., "GLAS PAD Calibration Using Laser Reference Sensor Data," *AIAA/AAS Astrodynamics Specialist Conference and Exhibit*, Vol. 1, A Collection of Technical Papers, AIAA, Reston, VA, 2004, pp. 302–311; also AAS Paper 2004-4857.

[20] Markley, F. L., "Attitude Error Representation for Kalman Filtering," *Journal of Guidance, Control, and Dynamics*, Vol. 26, No. 2, 2003, pp. 311–317.
doi:10.2514/2.5048

[21] Pittelkau, M. E., "Rotation Vector in Attitude Estimation," *Journal of Guidance, Control, and Dynamics*, Vol. 26, No. 6, 2003, pp. 855–860.
doi:10.2514/2.6929

[22] Savage, P. G., "Strapdown Inertial Navigation Integration Algorithms Design Part 1: Attitude Algorithms," *Journal of Guidance, Control, and Dynamics*, Vol. 21, No. 1, 1998, pp. 19–28.
doi:10.2514/2.4228

[23] Smith, N., Bae, S., and Schutz, B. E., "Biased Star Tracker Measurements of Forty-Nine Stars from Flight Data," *Journal of Spacecraft and Rockets*, Vol. 47, No. 6, 2010, pp. 1023–1028.
doi:10.2514/1.49412

[24] Smith, N., Fowell, R., Bae, S., and Schutz, B. E., "Improved Star Tracker Instrument Magnitude Prediction from ICESat Flight Telemetry," *AAS Guidance and Control Conference, Advances in the Astronautical Sciences*, Vol. 141, Univelt, San Diego, CA, 2011, pp. 639–654; also AAS Paper 2011-086.

[25] Fowell, R. A., Smith, N., Bae, S., and Schutz, B. E., "Bad Stars," *AAS Guidance and Control Conference, Advances in the Astronautical Sciences*, Vol. 133, Univelt, San Diego, CA, 2009, pp. 20–36; also AAS Paper 2009-012.

[26] Smith, N., Bae, S., and Schutz, B. E., "Forty-Nine Biased Star Positions from ICESat Flight Data," *20th Spaceflight Mechanics Meeting, Advances in the Astronautical Sciences*, Vol. 136, Univelt, San Diego, CA, 2010; also AAS Paper 2010-205.

[27] Magill, D., "Optimal Adaptive Estimation of Sampled Stochastic Processes," *IEEE Transactions on Automatic Control*, Vol. 10, No. 4, 1965, pp. 434–439.
doi:10.1109/TAC.1965.1098191

[28] Hanlon, P. D., and Maybeck, P. S., "Multiple-Model Adaptive Estimation Using a Residual Correlation Kalman Filter Bank," *IEEE Transactions on Aerospace and Electronic Systems*, Vol. 36, No. 2, 2000, pp. 393–406.
doi:10.1109/7.845216

[29] Alsuwaidan, B. N., Crassidis, J. L., and Yang, C., "Generalized Multiple-Model Adaptive Estimation Using an Autocorrelation Approach," *IEEE Transactions on Aerospace and Electronic Systems*, Vol. 47, No. 3, 2011, pp. 2138–2152.
doi:10.1109/TAES.2011.5937288

[30] Schutz, B. E., Bae, S., Smith, N., and Sirota, J. M., "Precision Orbit and Attitude Determination for ICESat," *F. Landis Markley Astronautics Symposium, Advances in the Astronautical Sciences*, Vol. 132, Univelt, San Diego, CA, 2008, pp. 775–791; also AAS Paper 2008-305.